

2

ULTRAFAST SCANNING ELECTRON MICROSCOPY

Ultrafast scanning electron microscopy (USEM), based on a laser-driven electron source, is a promising technique for the study of material dynamics at the nanoscale. While ultrafast TEMs have been widely discussed and characterized, work on ultrafast SEMs (USEM) is still limited. In this chapter we provide a full overview of a USEM based on the photoemission of electrons upon fs laser excitation of a Schottky field-emission gun. We start by discussing the fundamentals of electron emission in continuous and pulsed conditions and the main parameters involved in each process. Next, we focus on the technical aspects of our USEM, including the alignment procedure. Finally, we develop a full characterization of our setup. We present measurements of the electron energy distribution in USEM for different emission conditions and we show its dependence on the number of electrons per pulse. The energy spread ranges from 0.77 (< 1 electron per pulse) to 14.4 eV (~ 1000 electrons per pulse), with the latter dominated by Coulomb repulsion between electrons. We estimate an electron pulse width of 416 fs in the case of low number of electrons per pulse, and 6.4 ps for pulses containing ~ 1000 electrons. The spatial resolution (~ 90 nm) is evaluated for different settings in the emission process and we discuss the main factors that can lead to a higher spatial resolution.

2.1. INTRODUCTION

Ultrafast electron microscopy (UEM) has emerged as a powerful tool to study material dynamics combining high temporal (typically tens or hundreds of femtoseconds) and spatial (~ nm, down to Å in TEMs) resolution [43, 96–98]. One of the main techniques to obtain a pulsed electron beam is through photoemission of electrons upon excitation of the electron cathode with femtosecond laser pulses. This method results in a high temporal resolution, similar to that of optical exper-

iments, and enables pump-probe studies, in which the same laser is used to excite the sample, while the electrons act as a probe. Some examples of works using laser-driven electron sources in TEMs are the study of the dynamics of structural changes [61, 97], phase transformations [86, 99], optical near fields [87, 89] and off-axis electron holography [100], among others. In SEMs, applications include the investigation of photoinduced carrier dynamics in semiconductors [75, 90] and time-resolved cathodoluminescence [72, 79]. Pulsed electron beams can also be obtained using a beam blanker, in which the electron beam is swept over an aperture, but typically results in lower temporal resolution (~ 30 ps) [44, 49] and is less suitable for pump-probe measurements.

A complete understanding of the resolution and limitations of pulsed electron beams is critical for optimum performance of an UEM. The characterization of laser-driven sources in TEMs has been addressed in several works, in which the temporal, spatial and energy resolution was analyzed [44, 63, 65–67, 101]. The effects of Coulomb interaction (space-charge effects) are also discussed in literature, showing that the performance of UTEMs is strongly dependent on the average number of electrons per pulse [64, 102, 103]. In contrast, the literature on characterization of ultrafast SEMs (USEM) is more limited, and has mainly focused on temporal and spatial resolution [98, 104]. Even though the photoemission process is mostly dependent on the electron cathode (planar, LaB₆, Schottky FEG or cold-FEG), differences in the electron column between TEM and SEMs can also play a role in the characteristics of the electron pulses on the sample. Moreover, the final application of the pulsed electron beam is different in both cases, thus it is important to analyze and discuss the features of the pulsed beam specifically to SEMs.

In this chapter we provide a full characterization of an ultrafast SEM, based on a laser-driven Schottky FEG. We start by reviewing the fundamentals of electron emission in normal (continuous) and pulsed mode, and we present the technical design and development of our USEM, which is based on a commercial SEM. We operate the USEM in two different regimes, containing either a low (< 1) or high (up to 1000) average number of electrons per pulse. We discuss the impact of the different emission regimes and microscope settings on the energy spread of electron pulses in continuous and pulsed mode, and on the temporal and spatial resolution of the USEM.

2.2. CONTINUOUS EMISSION OF ELECTRONS

Before discussing the characterization of a pulsed electron source, it is important to understand the working principle of an electron source in normal conditions, that is, to obtain a continuous electron beam. Here we briefly review the main types of electron sources and characteristic features.

2.2.1. ELECTRON SOURCES

Standard electron microscopes, both SEM and TEMs, use micro and nanotips as electron sources. A secondary electron (SE) image of such nanotip is shown in Fig.

	LaB₆ (TE)	W (TE)	Shottky FEG	Cold FEG
Material	LaB ₆	W	ZrO/W [100]	W [310]
ϕ (eV)	2.4-2.7	4.5	2.8-2.92	4.25-4.5
T (K)	1700	2700	1800	300
E_{ext} (Vm ⁻¹)	-	-	$\sim 10^8$	$> 10^9$
I_e (A)	$\sim 10^{-3}$	$\sim 10^{-3}$	$\sim 10^{-4}$	$\sim 10^{-5}$
B (Am ⁻² sr ⁻¹)	$\sim 10^{10}$	$\sim 10^9$	$\sim 10^{11} - 10^{12}$	$\sim 10^{13} - 10^{14}$
ΔE_0 (eV)	1-2	1.5-3	0.5-1	0.2-0.4
Pressure (Pa)	$\sim 10^{-4}$	$\sim 10^{-2}$	$\sim 10^{-7}$	$\sim 10^{-9}$

Table 2.1: Main types of electron sources with the corresponding parameters. TE refers to thermionic emission and FEG to field-emission gun. ϕ is the work function, T is the operating temperature, E_{ext} refers to the magnitude of the extractor field, I_e is the total emitted current, B is the brightness, ΔE_0 is the energy spread and pressure refers to the vacuum pressure at which the source operates. Data extracted from refs. [8, 43].

2.1a (reproduced from [105]), corresponding to a tungsten cathode with a ZrO coating (ZrO/W), typically used in Schottky FEGs, as will be discussed below.

There are three main types of electron sources, depending on how electrons are released from the tip: thermionic, Schottky and cold field-emission [8]. Each of them offers its own advantages and disadvantages. Table 2.1 shows an overview of the different types of electron sources and their main properties: work function (ϕ), working temperature (T), amplitude of the extractor field (E_{ext}), emitted current (I_e), brightness (B), electron energy spread (ΔE_0) and pressure at which the source operates. The work function of the material is defined as the work needed to release an electron from the material to the vacuum [106], while the brightness of an electron source is defined as

$$B = \frac{I_e}{A_s \Omega}. \quad (2.1)$$

Here, I_e is the total current emitted by the source, A_s is the emitting area and Ω is the solid angle in which electrons are emitted [8]. The brightness of a source determines the trade-off between electron current, spatial resolution and coherence of the electron beam [107].

THERMIONIC SOURCE

In thermionic emission, the temperature of the tip is increased through Ohmic heating, such that electrons acquire energy to overcome the work function and be released from the tip. The two main materials used for thermionic emission are LaB₆ and W, with work function corresponding to 2.4 – 2.7 eV and 4.5 eV, respectively (see Table 2.1). Figure 2.1b shows the Fermi-Dirac distribution of electrons in a material for a temperature of 0 (black) and 1800 K (dark red). Here the probability that a given energy state is occupied, $f(E)$, is given on the x-axis as a function of the energy (y-axis). In the limit of 0 K, the occupation probability of any state with energy larger than the Fermi level is zero, and thus no electron emission is possible.

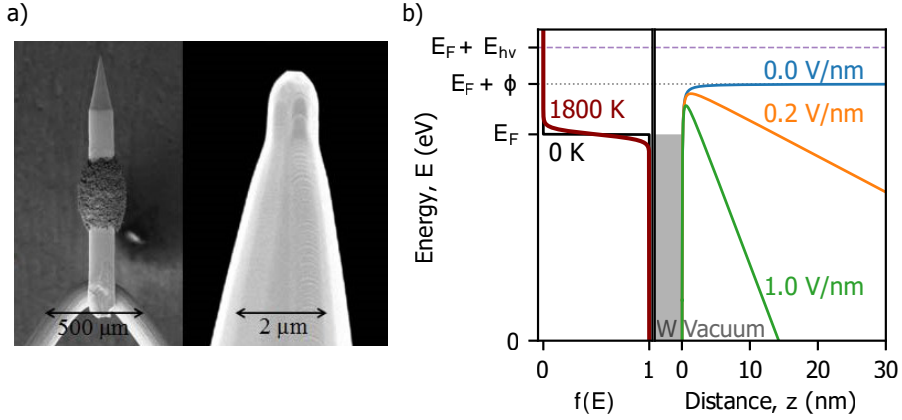


Figure 2.1: Emission of electrons from an electron cathode. (a) SE image of a typical ZrO/W nanotip, showing the ZrO reservoir (left) and the apex of the tip (right). Reproduced from [105]. (b) (left) Fermi-Dirac distribution of electrons in the electron source for different energy states at a temperature of 0 K and 1800 K. (Right) Energy barrier of an electron as a function of its distance to the surface of the tip, calculated for an applied external electric field of 0, 0.2 and 1 V nm⁻¹ (blue, orange and green, respectively). ϕ is the work function of the tip, and E_{hv} refers to the energy of a photon in the case of a laser-driven source.

Increasing the temperature of the tip leads to an increase of the occupation probability of higher energy states, thus allowing for emission of electrons (thermionic emission). Thermionic sources typically exhibit brightness of $10^9 - 10^{10}$ A m⁻² sr⁻¹ and energy spreads in the 1 – 3 eV range (Table 2.1).

SCHOTTKY FEG

The energy needed for electrons to escape from the tip can be further reduced by means of the Schottky effect [107]. In this case, a positive bias voltage is applied relative to the emitter, which we will refer to as extractor voltage (V_{ext}). The presence of an electric field (E_{ext}) around the tip effectively lowers the energy barrier. We can describe this effect theoretically by considering the potential energy of an electron that has been released from the tip. The electron leaves a positive screening charge behind, and thus experiences a restoring force due to Coulomb attraction. The potential energy associated to this positive-negative charge configuration can be calculated by considering the work needed to bring a charge from infinity to the position z . Hence, the potential energy of an electron right outside of the cathode in the presence of an external electric field E_{ext} can be approximated as [105]

$$U_E(z) = E_F + \phi - \frac{k_e q^2}{4z} - qE_{\text{ext}}z, \quad (2.2)$$

where E_F is the Fermi energy, ϕ the work function of the material, k_e the Coulomb constant, q the electron charge and z represents the distance from the surface of the electron cathode. Figure 2.1b (right) shows the potential energy of an electron

right after escaping the tip when no external voltage is applied (blue curve), as well as for $E_{\text{ext}} = 0.2$ and 1.0 Vnm^{-1} (orange and green, respectively). In the absence of an external electric field, the energy barrier, defined as the difference between the maximum potential energy and the Fermi level, corresponds to the work function of the tip, and emission is purely thermionic. This barrier is lowered by 0.54 and 1.2 eV for $E_{\text{ext}} = 0.2$ and 1.0 Vnm^{-1} , respectively. Additionally, the energy barrier also becomes narrower for increasing extractor field, thus allowing for quantum tunnelling of electrons with energy lower than the work function.

An electron source using this combination of thermionic emission and the Schottky effect is referred to as a Schottky field-emission gun (FEG). These sources typically use a W tip with ZrO coating, which reduces the work function of the material down to $\sim 2.9 \text{ eV}$ [65, 105]. The application of high extractor fields on the nanotip of Schottky FEGs results in higher brightness than thermionic sources ($\sim 10^{11} - 10^{12} \text{ Am}^{-2} \text{ sr}^{-1}$), due to the reduced emitting area. The lower operating temperature also results in a lower electron energy spread ($\sim 0.5 - 1 \text{ eV}$), due to the reduced excess energy of the emitted electrons (Table 2.1). This type of electron source is the one used in this thesis.

COLD FEG

Finally, field-emission guns can also operate without heating the tip, i.e., at room temperature. In this case, the extractor field applied to the nanotip is larger than in the Schottky FEGs, and emission is possible through quantum tunneling of electrons with energy close to the Fermi energy to the vacuum [43]. This allows one to achieve a higher brightness ($\sim 10^{13} - 10^{14} \text{ Am}^{-2} \text{ sr}^{-1}$) and lower energy spread ($\sim 0.2 - 0.4 \text{ eV}$) than the sources discussed above. These features make cold-FEGs desirable for applications in scanning transmission electron microscopy, such as EELS.

2.2.2. GEOMETRY OF A SHOTTKY FEG

In this thesis we use an SEM equipped with a Schottky FEG source. A schematic of the Schottky FEG geometry can be seen in Figure 2.2a (top left). Here, the ZrO/W tip is surrounded by a negatively biased plate (suppressor), from which it protrudes by about $250 \mu\text{m}$. In our case, the suppressor voltage is fixed to -500 V . The presence of this negative voltage ensures that only electrons from the end of the tip can be released to the vacuum. The extractor plate, which is positively biased (4550 V), is placed at around $500 \mu\text{m}$ from the apex of the tip and has a central aperture through which electrons can go through [105]. We should note that the typical values of extractor voltage and distance between the emitter and extractor plate would lead to an extractor field much lower than the ones given in Figure 2.1b if a planar geometry of the electron source is assumed. However, the sharp apex of the tip produces an enhancement of the electric field, thus achieving a larger extractor field near the tip. The combination of extractor and suppressor voltages around the tip also has an impact on the brightness of the source, that is, the area of the tip from which electrons are emitted, and their direction. In particular, lowering the extractor volt-

age with respect to the suppressor voltage results in a decrease of the brightness, as will be discussed below. Hence, by tuning these voltages we can control how many electrons emitted away from the apex of the tip go through the extractor aperture and are thus collected [105]. Having control over it will allow us to choose between different photoemission regimes, as will be discussed below.

2.3. PULSED EMISSION OF ELECTRONS: LASER-DRIVEN SCHOTTKY FEG

Until now we have discussed the operation of a Schottky FEG in normal conditions, that is, to obtain a continuous electron beam. In the case of a laser-driven source, a pulsed laser beam is focused on the electron cathode and electrons are released from the tip through the photoelectric effect (photoemission). In this case, the tip is usually operated at a low temperature in order to suppress continuous emission. Hence, the energy needed to overcome the work function is provided by the photon energy instead of thermal excitation. In our case we use a laser beam with photon energy $E_{hv} = 4.82 \text{ eV}$ ($\lambda = 258 \text{ nm}$), which is much larger than the work function of ZrO/W (2.9 eV). Other works have demonstrated photoemission using lower photon energies, even below the ZrO/W work function, in which case the emission of electrons takes place by means of the absorption of two (or more) photons [108–110]. In the case of low photon energy and higher laser peak intensity ($I > 10^{12} \text{ W cm}^{-2}$) [108], the emission of electrons can also take place by optical field emission, in which the light field around the tip is strong enough to allow for tunneling of electrons. Multiphoton photoemission and optical field emission are not studied in this chapter.

Using a high photon energy has some significant advantages. During a typical experiment with a cold tip, the ZrO coating cannot be replenished due to its lower diffusivity, thus leading to an increase of the work function [105]. Using high energy photons allows us to still have efficient emission of electrons even when the work function is increasing due to the consumption of the ZrO coating [74]. In our experiments, we have observed that the photoemission efficiency, that is, the average number of electrons emitted per incoming laser photon, decreases by $\sim 30\%$ after $\sim 90 \text{ min}$, similar to other work [76]. This can be solved by briefly heating up the tip in between experiments. An additional advantage of using high energy photons is the fact that the reduction of the energy barrier by the extractor field is no longer needed. This gives us flexibility to lower the extractor voltage to achieve different working regimes while still having emission of electrons.

2.4. IMPLEMENTATION OF A USEM

Next, we present the technical details related to the development of our USEM, and we discuss a procedure to align the laser on the electron cathode.

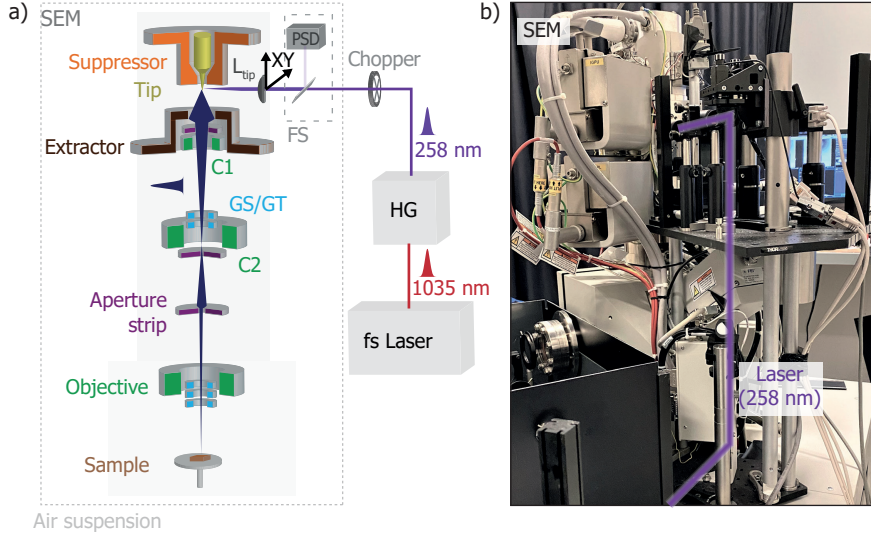


Figure 2.2: USEM based on a laser-driven Schottky FEG. a) Schematic of the setup. The 4th harmonic ($\lambda = 258\text{ nm}$) of a femtosecond laser, generated through a set of BBO crystals (HG), is focused on the electron cathode of the SEM. Alignment between the laser and the microscope is kept using a feedback system (FS). The electron cathode (tip) slightly protrudes from the suppressor plate ($\sim 500\text{ V}$). The emission of electrons is enhanced by the extractor plate (4550 V). The electron beam is further focused along the column using two condenser lenses, C_1 and C_2 , before reaching the final objective lens, which focuses the beam on the sample. GT/GS: gun tilt/shift, respectively. b) Photograph of the setup.

2.4.1. LASER-DRIVEN SEM SETUP

Figure 2.2 shows a schematic (a) and a photograph (b) of the setup that we use in our laser-driven electron microscope. The USEM has been developed from a standard Thermo Fisher Quanta 250 FEG SEM, with the exception of the initial measurements that used a Thermo Fisher/FEI XL30 (chapter 4). Access to the electron cathode is given through a UV-transparent window. A two-level breadboard has been attached to the electron microscope on which optical components are mounted. The breadboard configuration is thus coupled to the air suspension of the SEM, used to isolate the microscope from vibrations in the room. The alignment between this floating part of the setup and the rest of optical components, including the laser, is maintained by using an optomechanical feedback system (more details in Chapter 3, section 3.2).

We use a femtosecond laser (Clark MXR Impulse, diode-pumped Yb-doped fiber oscillator/amplifier system) providing $\sim 250\text{ fs}$ pulses, with tunable repetition rate ($200\text{ kHz} - 25.19\text{ MHz}$) and wavelength output at $\lambda \approx 1035\text{ nm}$. The fundamental laser beam is sent through a set of beta barium borate (BBO) crystals to produce the 2nd ($\lambda_{SH} = 517\text{ nm}$), 3rd ($\lambda_{TH} = 345\text{ nm}$) and 4th ($\lambda_{FH} = 258\text{ nm}$) harmonics. The 4th harmonic is used for the photoemission of electron pulses. We use a beam expander composed of two lenses (focal length 10 and 50 cm, respectively) to increase

the beam size of the 4th harmonic beam by a factor 5. The beam is guided up to the height of the electron cathode through a periscope. The top part of the periscope contains a dichroic mirror which reflects the 4th harmonic, while transmitting at longer wavelengths. Finally, the beam is focused on the electron cathode through a lens (tip lens, $f = 12.5\text{mm}$) down to a $\sim 10\mu\text{m}$ spot. The position of the lens in the direction of the optical axis (z) is adjusted using a manually controlled linear stage, while the position in the transverse direction (x, y) is controlled by means of two motorized stages (PI M-227).

ELECTRON COLUMN

The electron column is composed of the electron gun module, containing the suppressor and extractor voltage plates, together with the tip, as discussed in section 2.2. A $\sim 350\mu\text{m}$ -diameter aperture is placed below the extractor plate to block electrons emitted further away from the optical axis. A set of two condenser lenses, is used to change the position of the crossover the electron beam along the column, and the microscope contains a set of apertures (aperture strip, $30 - 1000\mu\text{m}$). The particular condenser lens voltages (C_1 and C_2) determine the fraction of the beam that goes through the aperture. Finally, an objective lens is used to focus the electron beam on the sample.

2.4.2. EXPERIMENTAL PROCEDURE TO FIND THE TIP

A critical step in performing time-resolved experiment with an electron microscope is the proper alignment of the laser on the electron cathode. The next sections show the typical procedure performed during the installation of the setup and prior to starting an experiment.

INITIAL ALIGNMENT OF THE LASER

The first alignment of the laser on the tip can be performed with the help of a CMOS camera and a set of irises. In normal operating conditions, the electron cathode is set to 1800 K and its blackbody radiation can be observed by eye. This radiation is collected by the lens in front of the SEM window ($f = 12.5\text{mm}$) and imaged on a CMOS camera (Thorlabs DCC1645C). In our case, we placed the CMOS camera behind the dichroic mirror from the periscope, and an achromatic lens ($f = 3\text{cm}$) was used to focus the light onto the camera. A photograph of the visible blackbody radiation of the tip is shown in Fig. 2.3a. This configuration allows us to roughly align the lens focus on the electron cathode. The focus is later optimized by maximizing the current emitted by the cathode, as explained below. In order to align the laser on the tip (in the transverse direction, x, y), we placed a set of two irises through which the emitted light goes. Then the laser is aligned such that it goes through the center of the irises, thus giving a rough alignment of the laser on the tip. The exact position of the laser beam with respect to the tip is optimized by scanning the lens in front of the tip with two motorized stages, as will be explained in the next section. We should note that this initial alignment procedure is only needed during the installation of the setup or after major changes in the laser beam path.

SCANNING OF THE LENS

Once the photoemission setup is fully installed, the steps presented in the previous section can be omitted. Hence, we only need to fine-tune the position of the laser on the electron cathode within a $\sim 100 \times 100 \mu\text{m}^2$ scanning window. It is usually desirable to start the alignment of the laser beam on the tip with a hot tip, that is, using the standard settings of the electron column. When lowering the temperature of the tip, it thermally contracts by up to a few tens of μm [105], which results in a change of the alignment of the electron beam path inside the column. Hence, starting the alignment of the laser on the cathode with a hot tip ensures an optimum collection of the photoemitted electrons. It is also helpful to optimize the parameters inside the electron column (gun tilt/shift, condenser lens voltage and aperture) for maximum collection of the electrons in continuous mode. We collect the electron current on the sample by focusing the electron beam on a Faraday cup, placed on the sample stage, which is connected to a picoammeter (Keithley 6485) or to a lock-in amplifier (Zurich Instruments MFLI, 500 kHz/5 MHz) through a current amplifier (Femto DLPCA-200). When the tip is hot (that is, working in continuous mode) most of the collected electron current comes from the continuous emission, even if the laser beam is already focused on the tip. However, modulating the 4th harmonic laser beam using an optical chopper (Hz - kHz) (Thorlabs MC2000B-EC), which is also connected to a lock-in amplifier, allows us to discern between continuous (field-enhanced thermionic emission) and pulsed (photoemission) electron currents. Additionally, it can be helpful to further tune the parameters inside the electron column (gun tilt/shift, condenser lens voltage and aperture) in order to maximize the collection of the photoemitted electrons.

Figure 2.3b shows a measurement obtained when scanning the tip lens around the electron cathode (in the x, y plane) and collecting the electron signal from the lock-in amplifier. In this case the Schottky FEG was operating in normal conditions (1800 K, $V_{\text{ext}} = 4550 \text{ V}$), the electron beam acceleration was set to 10 kV and the continuous (background) electron current was $\sim 200 \text{ nA}$ (using a 1 mm aperture). We used a laser power ($\lambda_{\text{FH}} = 258 \text{ nm}$) of 1.6 mW at 5.04 MHz (0.3 nJ/pulse). The gain of the current amplifier was set to 10^6 A V^{-1} and the chopping frequency was 287 Hz. We observe that photoemitted current is collected even when the laser is focused more than $60 \mu\text{m}$ away from the apex of the tip. The configuration of suppressor and extractor voltage ensures that only electrons emitted from the apex of the tip can be released and go through the extractor aperture, and it is thus unlikely that electrons far from the apex (shank emission) can be efficiently released. Instead, the current observed when focusing far from the apex of tip is probably due to emission of electrons from the apex that are excited by the tail of the laser beam profile (assumed to be Gaussian).

Once the laser is aligned on the tip, we lower the temperature of the tip to suppress continuous emission. This is done by decreasing the filament current from 2.35 A to 1.7 A, resulting in a final temperature of $\sim 1200 \text{ K}$. Figure 2.3c shows a scan of the tip lens obtained under the same conditions as in 2.3b, but at this lower temperature. Given the thermal contraction of the tip at this low temperature, here we

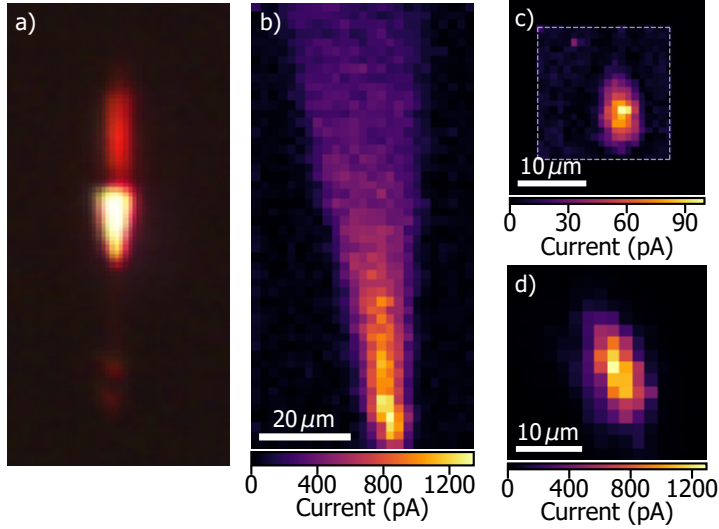


Figure 2.3: Experimental procedure to focus the laser on the electron cathode. (a) Photograph of black-body radiation of the tip under normal operating conditions ($T \approx 1800$ K). (b) Map of the pulsed current collected on a Faraday cup while scanning the laser focus around the hot tip in the xy plane ($T = 1800$ K, $V_{ext} = 4550$ V). The current produced by photoemission is distinguished from the continuous one using a lock-in amplifier. (c) Similar map as in (b) but with a colder tip ($T \approx 1200$ K). (d) Similar map as in (c) but obtained at $V_{ext} = 650$ V. Here the continuous emission is fully suppressed and the pulsed current is measured directly with a picoammeter.

realigned the electron column and adjusted the condenser voltage (C_1) for optimal electron collection. Here, C_1 was increased from 1125 V in normal conditions to 1190 V. We observe that the overall emission decreased by $\sim 92\%$, down to the tens of pA regime. Moreover, now emission can be observed only from a relatively small area, corresponding to the apex of the tip, due to the lower photoemission efficiency. Regardless of this reduction in the temperature of the tip, complete suppression of continuous emission is only achieved after letting the tip cool down for at least 1 h, which is not practical for experiments.

A way to instantaneously remove the remaining continuous emission is by lowering the extractor voltage, such that the effective work function of the ZrO/W tip is increased (Fig. 2.1b). We have observed that lowering the extractor voltage to ~ 3000 V results in the full suppression of continuous emission. Given that the photon energy of the laser beam is much larger than the work function, photoemission of electron pulses is barely affected. Further reducing the extractor voltage to 650 V results in an enhancement of the photoemitted electron current collected on the Faraday cup, as will be seen below (section 2.5.3), contrary to what we would expect from the Schottky theory explained in section 2.2. In normal operating conditions, the extractor-suppressor configuration acts such that a large fraction of the emit-

ted electrons are blocked by the extractor aperture. Instead, when the magnitude of the extractor voltage is similar to that of the suppressor, most of the emitted electrons can go through the aperture, thus increasing the collection efficiency of the photoemitted electrons [105]. Figure 2.3d shows a scan of the tip lens obtained at $V_{\text{ext}} = 650\text{ V}$. Given that there is not continuous emission anymore, the laser beam is not chopped and the electron current collected by the Faraday cup is sent directly to a picoammeter. Here again, the condenser lens was readjusted ($V_{\text{Cl}} = 650\text{ V}$) together with gun tilt and shift to maximize the collection of electrons. All other parameters were kept the same as in Fig. 2.3c. We observe that in this case the maximum electron current is 1.29 nA , corresponding to an average of ~ 1600 electrons per pulse. We should note that this corresponds to one of the lowest values of the extractor voltage at which photoemission is still possible. Lowering V_{ext} below the magnitude of the suppressor voltage (500 V) would result in the total suppression of emission of electrons from the tip.

2.5. ENERGY SPREAD OF THE ELECTRON BEAM

Electrons emitted from an electron cathode have an energy equal or close to the energy barrier, which is determined by the combined effect of work function of the tip and extractor field (in the case of a Schottky FEG). Electrons with energy larger than the energy barrier can be easily released, but the occupation probability of these higher energy states, given by the Fermi-Dirac statistics, is low. Instead, energy states below the energy barrier have a larger occupation probability, but electrons in these states can only be released through quantum tunneling. Hence, the emitted electrons have a certain energy distribution (ΔE), determined by the Fermi-Dirac statistics and the strength of extractor field [105]. Other parameters in the emission process, such as defects on the tip and slight changes of the work function for different facets of the tip, also contribute to the electron energy spread. Moreover, Coulomb repulsion, also referred to as space-charge effects, at the gun and, to a lesser extent, at the different crossovers along the electron column, can also play a role in the final electron energy width [111, 112]. This means that in experiments, electrons have an energy of $E_0 \pm \Delta E$, where E_0 is the operating energy ($E_0 \sim 0.5 - 30\text{ keV}$ for SEMs and $60 - 300\text{ keV}$ for TEMs).

The uncertainty in the energy of the electron beam is a crucial parameter in several analytical techniques such as electron-energy-loss spectroscopy (EELS), usually performed in (S)TEMs, given that it directly affects the energy resolution of the measurements. In SEMs, the energy spread can have a strong impact on the spatial resolution and, in the case of pulsed electron beams, also on the temporal resolution. Therefore, knowing the energy spread of the electron beam and the parameters that influence it is essential to optimize the performance of (time-resolved) SEMs.

2.5.1. RETARDING FIELD ANALYZER

The energy width of an electron beam in (S)TEMs is typically measured using an EELS detector, which is based on the controlled deflection of electrons depending on their energy by means of a magnetic prism. Here instead we use a retarding field energy analyzer (RFA) to measure the energy spread for low-energy electron beams in the SEM. The RFA was obtained from Prof. P. Kruit (Technical University of Delft) and is based on the work by M. van der Heijden [113]. A schematic of the setup is shown in Fig. 2.4a. The RFA is mounted on the sample stage of the SEM (see photograph, Fig. 2.4b) and the electron beam is directly sent through an initial aperture, after which it is focused on the retarding electrode (orange in the figure). The voltage on this electrode (V_{RF}) is supplied by a fixed negative offset voltage V_{offset} , usually set slightly below the electron accelerating voltage (-5 kV), plus a tunable small (negative) voltage ΔV in the range of a few tens of volts. Our RFA is designed to operate at an electron accelerating voltage of $V_0 = -5$ kV. Hence, when $V_{RF} = V_{\text{offset}} + \Delta V < V_0$ most electrons will go through the electrode and end up being collected by a Faraday cup, which is connected to an electrometer (Keithley 6514 System Electrometer). Instead, when $V_{RF} > V_0$ most electrons will be repelled and will not reach the Faraday cup. In an experiment, ΔV is scanned and the current collected by the Faraday cup in each step is recorded. Hence, the dependence of the collected current on V_{RF} directly gives the electron energy distribution, given the relation $E = qV$ (with q the electron charge). An additional negative voltage (-9 V) is also set at the entrance of the Faraday cup to hinder the escape of secondary electrons created in the Faraday cup.

Figure 2.4c shows a measurement performed with a 5 keV continuous electron beam, obtained using a 40 μm diameter aperture. The figure shows the current I collected by the Faraday cup as a function of the potential energy on the retarding field electrode, defined as $E_{RF} = qV_{RF}$. Here V_{offset} is set to ~ -4.99 kV and ΔV is scanned over a 0 to -15 V range with step size of 117 mV. We fit the data with the cumulative distribution function (CDF) of a pseudo-Voigt distribution (V_p), defined as

$$\begin{aligned}
 I(E) &= V_p(E; I_0, k, E_c, \gamma, B) = \\
 &= kL(E) + (1 - k)G(E) + B = \\
 &= -k \frac{I_0}{2} \left[\frac{1}{\pi} \arctan \left(\frac{E - E_c}{\gamma} \right) + 1 \right] + \\
 &\quad + (1 - k) \frac{I_0}{2} \left[1 - \text{erf} \left(\frac{\sqrt{\log 2}}{\gamma} (E - E_c) \right) \right] + B,
 \end{aligned} \tag{2.3}$$

where $L(E)$ is the CDF of a Cauchy-Lorentz distribution with width parameter γ and $G(E)$ is the CDF of a normal distribution with standard deviation $\sigma = \sqrt{2 \log 2} \gamma$. Both CDFs are centered around E_c , and have amplitudes proportional to the total electron current I_0 . The parameter k indicates the contribution of each CDF to the measured curve, and B a background, representing the noise level of the measurement. The red curve in Fig. 2.4c is the fit of the data, obtained with $\gamma = 0.39$ eV, $I_0 = 2.12$ pA, $E_c = 6.14$ eV and $k = 0.13$. The energy spread of the electron beam is

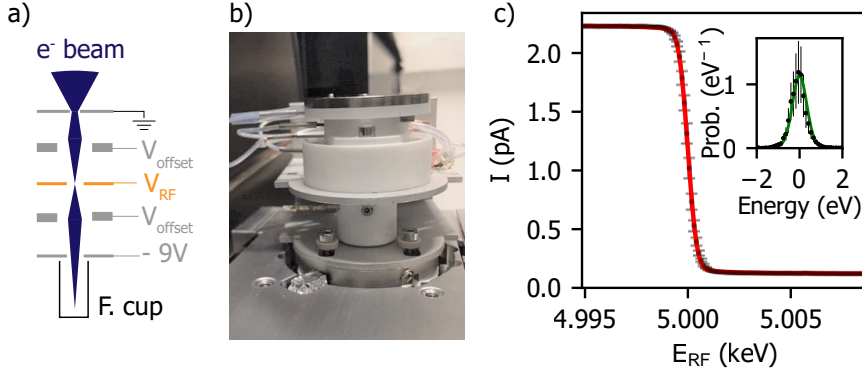


Figure 2.4: Energy-spread measurements with the retarding field analyzer (RFA). (a) Schematic of the RFA setup: the electron beam is accelerated up to V_{offset} , typically set slightly below the operating voltage of the SEM (~ 5 kV). The beam is focused on the retarding electrode, set at $V_{\text{RF}} = V_{\text{off}} + \Delta V$, and ΔV is scanned over a fixed voltage range, typically from 0 to -30 V. The electrons that go through the electrode are collected in the Faraday cup. Escape of secondary electrons from the Faraday cup is hindered by setting a negative potential (-9 V). (b) Photograph of the RFA setup mounted on the sample stage of the SEM. (c) RFA measurement of the energy spread of a 5 keV continuous electron beam. The red curve represents a fit obtained when using a pseudo-Voigt distribution. Inset: electron energy distribution, obtained from the derivative of the RFA data, together with the probability density function of a pseudo-Voigt function (green).

defined as $\Delta E = 2\gamma$, corresponding to the full width at half maximum of the curve, which in this case is $\Delta E = 0.79$ eV. We should note that in the plot, E_c has already been subtracted from the x-axis, such that the center corresponds to the electron beam energy. The precise value of V_{offset} is not known, given the limited precision of the high voltage supply readout, thus the exact ΔV at which $E_{\text{RF}} = 5$ keV is always extracted by subtracting the fitted value of E_c from the electron energy E_0 , thus assuming that the center corresponds to E_0 .

The derivative of the RFA data with respect to the retarding field energy gives the shape of the energy distribution of the electron beam. The result is shown in the inset of Fig. 2.4c. Given that the noise is amplified when performing the derivative, it is best to fit the data directly with Eq. 2.3 rather than fitting its derivative (green curve in the inset).

2.5.2. ENERGY SPREAD OF A CONTINUOUS BEAM

Several parameters have an impact on the energy distribution of a continuous electron beam. Here we evaluate how the emission conditions at the Schottky gun influences the final energy spread of the electron beam. The initial energy spread of the emitted electrons (ΔE_0) and the current emitted from the tip ($\sim 300 \mu\text{A}$) are determined by the tip temperature and suppressor and extractor voltages. In typical operating conditions (continuous emission), we have $T \sim 1800$ K, $V_{\text{supp}} = -500$ V and $V_{\text{ext}} = 4550$ V. The initial electron beam is cut through a set of apertures along

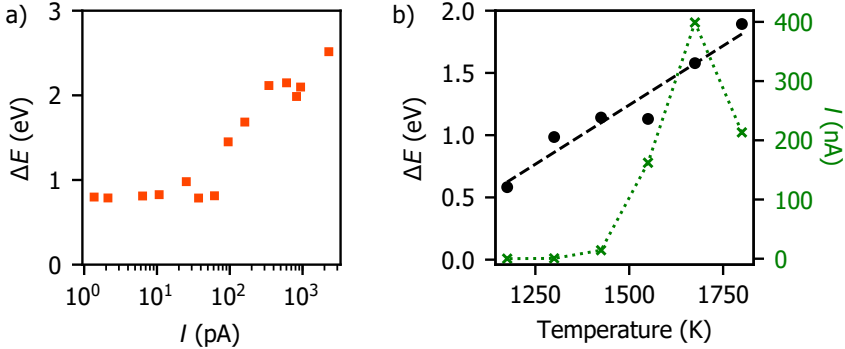


Figure 2.5: Energy spread of a continuous electron beam. (a) Energy spread (ΔE) of a 5 keV continuous electron beam as a function of the electron current collected on the Faraday cup. (b) Energy spread of the electron beam (black) and collected current I (green) as a function of the temperature of the tip.

the microscope column, which result in lower electron currents on the sample plane. Figure 2.5a shows the energy spread of the electron beam as a function of the electron current collected on the Faraday cup (that is, in the sample plane). The electron current is tuned by changing the value of the condenser lenses (C_1 and C_2), which determine the fraction of electrons that go through the final aperture ($40\text{ }\mu\text{m}$ in this case). We observe that reducing the current from 6.5 nA to 59 pA results in a decrease of the energy spread from 2.74 to 0.72 eV . This dependence of ΔE on the electron current can be due to two effects. First, when reducing the current we remove electrons that are emitted further away from the optical axis, that is, coming from different positions from the tip that might have slightly different work functions [105]. Second, at larger electron currents, Coulomb repulsion at the different crossovers along the microscope column can become more dominant, thus resulting in an increase of the energy distribution, as will be discussed in section 2.5.3.

Another parameter that affects the electron energy spread is the temperature of the electron cathode. As explained in section 2.2, decreasing the temperature of the emitter also reduces the occupation probability of higher energy states, thus decreasing the energy spread of the emitted electrons. Figure 2.5b shows the value of the energy spread measured as a function of the temperature of the tip. In each measurement the value of the condenser lens C_1 is changed in order to maximize the collected electron current, and we used the largest aperture (1 mm). We find that the energy spread decreases linearly with temperature, with a slope of 2 eVK^{-1} , from a value of 1.86 eV for a temperature of 1800 K , corresponding to the typical operating conditions of our Schottky FEG, down to 0.59 eV for 1175 K . At lower temperatures, the electron current reaching the sample becomes too unstable to give reliable results. We typically waited up to 40 min in between measurements to let the electron current stabilize.

In the figure we also plot the maximum electron current I collected on the Fara-

day cup as a function of the tip temperature. The current exhibits a decrease when reducing the temperature, as expected due to the lower occupation of high energy states at low temperature [8, 107]. The fact that the electron beam current at $T = 1800\text{ K}$ is lower than at 1675 K is attributed to non-optimum alignment of the electron column in the 1800 K case. Nevertheless, the energy spread is still lower at 1675 K than at 1800 K , thus further suggesting that the main effect on the energy spread comes from the change in temperature rather than the change in the value of the electron current measured on the Faraday cup.

2.5.3. ENERGY SPREAD OF A PULSED ELECTRON BEAM

Next, we evaluate the energy spread of pulsed electron beams obtained through photoemission. Similar to the continuous case, the initial energy distribution of electrons (ΔE_0) is determined by the electron gun conditions (temperature, extractor voltage). However, now the laser wavelength also plays a role: the excess of energy between the photon energy and energy barrier of the tip also contributes to the initial energy spread of the electron beam [114]. Moreover, in the case of ultrashort pulses, Coulomb repulsion in dense electron bunches becomes a critical factor, as will be discussed below.

In a typical photoemission experiment, electrons are emitted from a small area on the tip ($\sim \mu\text{m}$), governed by the size of the tip apex and extractor-suppressor configuration, and within a short time (usually a few hundreds of fs). This spatial and temporal concentration of electrons can lead to significant Coulomb interactions (space-charge effects), both in the lateral/transverse and longitudinal/axial directions, with respect to the electron beam propagation. In the first case, the main effect is a reduction of the spatial resolution, due to the spatial broadening of the electron beam. In the second case, referred to as Boersch effect, Coulomb repulsion among electrons within the same pulse leads to a broadening of the electron kinetic energy distribution [115]. The initial energy distribution of electrons (ΔE_0) translates into a difference in electron speed, and thus position along the optical axis. Coulomb repulsion will increase this broadening, given that the leading electrons will be further accelerated, while the electrons in the tail will experience a deceleration [105, 115–117]. This effect results in a gradual broadening of the energy width with increasing number of electrons per pulse, as previously reported in literature [102, 103]. Moreover, in the extreme case in which each pulse contains a large number of electrons, this effect can result in the appearance of two distinguished energy peaks, corresponding to the accelerated and decelerated electrons [101–103, 118].

In order to investigate the effect of Coulomb repulsion under different photoemission conditions, we performed RFA measurements of the energy spread as a function of the number of electrons per pulse (N_e). Figures 2.6a-b show two examples of such curves, obtained for an average value N_e of 0.53 and 1029 electrons per pulse, respectively. Here the current measured on the Faraday cup, and thus, N_e , was tuned by varying the laser power focused on the tip, corresponding to 4.23 and 273.41 pJ per pulse, respectively, in these particular cases. All other settings of

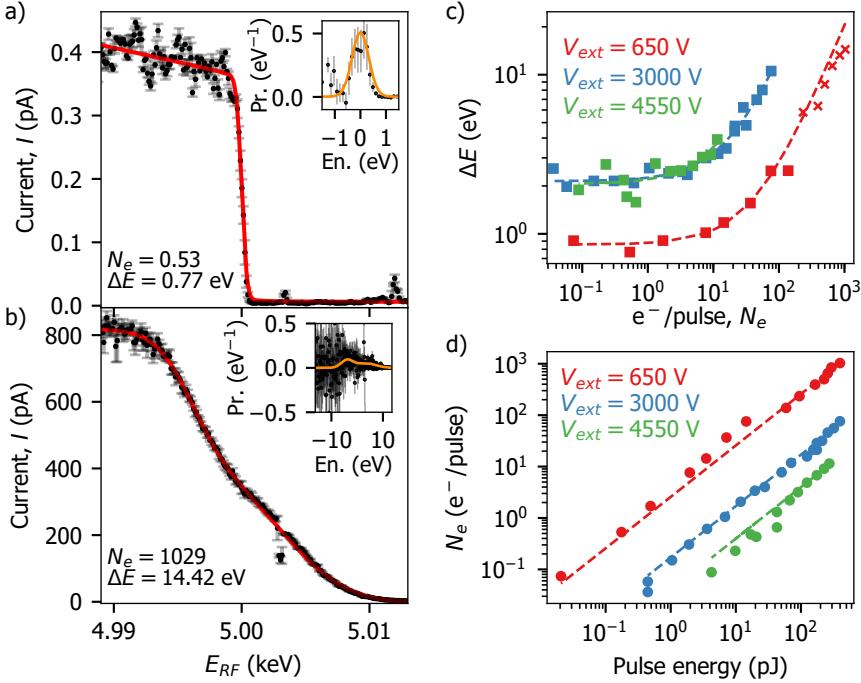


Figure 2.6: Energy spread of a pulsed electron beam. (a, b) RFA measurements obtained for a low (0.53) and high (1029) average number of electrons per pulse, obtained at 5 keV, and using a low extractor voltage ($V_{ext} = 650$ V). The solid red curves represent the fits using a single (a) and double (b) pseudo-Voigt distributions. The insets show the energy distributions obtained from the data, together with the analytical curves calculated from the results of the fits (orange). (c) Energy spread vs number of electrons per pulse for high (4550 V), medium (3000 V) and low (650 V) extractor voltages. The dashed lines are linear fits of the data. (d) Number of electrons per pulse collected on the sample plane as a function of the laser energy per pulse ($\lambda_{exc} = 258$ nm), together with the corresponding linear fits (dashed curves).

the electron column were kept the same, and the repetition rate of the laser was set to 5.04 MHz. In both cases the tip was cooled down ($I_{fil} = 1.7$ A, $T \approx 1200$ K), and we used $V_{ext} = 650$ V and $C_1 = 450$ V. We observe that the curve corresponding to $N_e = 0.53$ electrons per pulse (Fig. 2.6a) exhibits a sharp transition in the RFA spectrum. Fitting the curve with Eq. 2.3 (red curve) yields an energy spread of 0.77 eV. The curve also exhibits a linear downward trend in the $E_{RF} = 4.990 - 4.998$ keV range, where we would expect a constant current, which is attributed to a decrease of the electron current during the acquisition, probably due to drifting of the position of the laser beam with respect to the tip. This is accounted for in the fit. The inset in Fig. 2.6a shows the derivative of the data, together with the derivative from Eq. 2.3, calculated using the results from the fit.

In contrast, Fig. 2.6b shows the RFA measurement obtained for a very large number of electrons per pulse ($N_e \approx 1029$). In this case we observe a broadening of

the curve, corresponding to a larger energy spread, as expected from the Boersch effect. Moreover, we observe that the transition from high (800 pA) to zero current is not completely smooth but exhibits two features. This curve is best described when considering that the current collected by the Faraday cup as a function of the energy on the retarding field electrode depends on two pseudo-Voigt distributions, each centered around $E_{c,i}$ and with width parameter γ_i ($i = 1, 2$), that is,

$$I(E) = \eta V_p(E; I_0, k, E_{c,1}, \gamma_1, 0) + (1 - \eta) V_p(E; I_0, k, E_{c,2}, \gamma_2, 0) + B, \quad (2.4)$$

with the expression for V_p given in Eq. 2.3. Here the parameter η determines the contribution of each individual pseudo-Voigt function. The curve in Fig. 2.6b was best fitted when $k = 0$, meaning that the peaks are fully Gaussian, $\eta = 0.52$, $\gamma_1 = 2.62$ eV, $\gamma_2 = 4.56$ eV, $E_{c,1} = -3.92$ eV and $E_{c,2} = 3.32$ eV. Here the zero in the x-axis, which would correspond to $E_{RF} = 5$ keV, cannot be calculated directly from the fits, given that we have two values of E_c . Instead, we took the value from the curves that do not show a double peak, thus having a clear E_c . $E_{c,1}$ and $E_{c,2}$ are thus expressed with respect to this central energy. Moreover, the energy width ΔE of the electron beam is now defined as,

$$\Delta E = \gamma_1 + \gamma_2 + |E_{c,1} - E_{c,2}|. \quad (2.5)$$

The presence of these two peaks can be interpreted as a further proof of the contribution of Coulomb repulsion to the final electron energy distribution of highly dense electron pulses.

Figure 2.6c shows ΔE as a function of N_E obtained for three different extractor voltages: low ($V_{ext} = 650$ V, red), medium ($V_{ext} = 3000$ V, blue) and high ($V_{ext} = 4550$ V, green). The squares indicate the cases in which the data was fitted with a single pseudo-Voigt function, hence $\Delta E = 2\gamma$, while the crosses denote the cases in which a double pseudo-Voigt function was used, with energy spread calculated using Eq. 2.5. The energy spread gradually increases when increasing the number of electrons per pulse, as we would expect from the Boersch effect. We fit the data using a linear function (dashed curves), with slopes corresponding to 0.02, 0.11 and 0.15 eV/e⁻, for low, medium and high extractor respectively. These values indicate that the energy spread is more strongly affected by N_e in the high and medium extractor cases. This could be explained by the fact that for high extractor voltages, the extractor aperture blocks a large fraction of the photoemitted electrons. Hence, the same number of electrons collected on the sample plane corresponds to a larger number of photoemitted electrons in the high and medium extractor cases.

To investigate the collection efficiency of emitted electrons at different extractor voltage, Figure 2.6d shows the number of electrons per pulse collected on the Faraday cup as a function of the laser energy focused on the tip. The number of electrons emitted by the tip is higher than the values measured on the Faraday cup, given that the extractor aperture and rest of apertures along the microscope column block a fraction of the electron beam. In all cases the data in Fig. 2.6d can be fitted with a linear function, with slope 2.57, 0.17 and 0.04 e⁻ / pJ for low, medium and high extractor voltages, respectively. Hence, we observe again a clear difference between

the low and medium/high extractor cases. This result is initially counter intuitive, given that at lower extractor voltage the energy barrier is larger and, thus, we would expect that the electron emission efficiency is lower. However, the extractor voltage also has an impact on the collection efficiency. At low extractor voltage, the angular spread of electrons right after emission is lower than at high extractor voltage. Hence, fewer electrons are blocked by the extractor aperture, thus increasing the collection efficiency of photoemitted electrons. These results are compatible with the effect of the extractor voltage discussed in ref. [105].

Finally, we should note that we obtain the smallest energy spread when using a low extractor voltage, as seen in Fig. 2.6c. In particular, from the linear fits we extracted lower limits of 0.86, 2.14 and 2.05 eV (low, medium and high V_{ext}). These values represent the value of energy spread in the limit of low N_e , that is, with pulses containing less than one electron. In these cases Coulomb repulsion does not play a role, and the energy spread is determined by the conditions of photoemission. The lower energy spread obtained in the case of a low extractor voltage could be explained by the fact that lowering this voltage results in an effective increase of the energy barrier for the emission of electrons from the electron cathode. Hence, less electrons have excess energy, thus reducing the initial energy distribution. At a high extractor voltage ($V_{\text{ext}} = 4550\text{V}$), the energy barrier is lowered by $\sim 1\text{eV}$ (Eq. 2.2, $E_{\text{ext}} \sim 0.7\text{Vnm}^{-1}$), close to the difference in energy spread obtained here between high and low extractor voltages.

2.6. SPATIAL RESOLUTION

In the geometry of the laser-driven cathode, we drastically change the way electrons are emitted from the tip with respect to the continuous beam configuration. However, in principle the settings of the electron column itself can be kept the same as in continuous mode, which implies that fundamentally a similar spatial resolution can be achieved. Indeed, several reports have shown spatial resolutions down to 5 nm in a pulsed-laser driven SEM [90] and a resolution of 0.9 nm in TEM, in which a new laser driven cathode system using a cold-FEG was demonstrated [66]. Nevertheless, in practice several parameters in the electron column are usually adjusted, which can affect the spatial resolution. Here we discuss which parameters play a role in the spatial resolution and the different regimes in which we can work.

In the rest of this chapter we evaluate the spatial resolution by using a sample containing Sn spheres with diameters ranging from 50 nm up to 10 μm . All images are taken at the same working distance at which cathodoluminescence (CL) experiments are performed (14 mm), but without the CL mirror in place, as it blocks part of the SE emission. In all cases we use the 4th harmonic of the laser ($\lambda_{\text{exc}} = 258\text{nm}$) and the repetition rate is set to 25.19 MHz. We evaluate the spatial resolution (η) by means of the Fourier transform method presented in ref. [49]. We should note that differences in the electron beam focus and alignment of the column between experimental sessions have an impact on the exact value of η . Moreover, different levels of noise in the images, depending on the magnitude of the SE signal, also affect the accuracy of η .

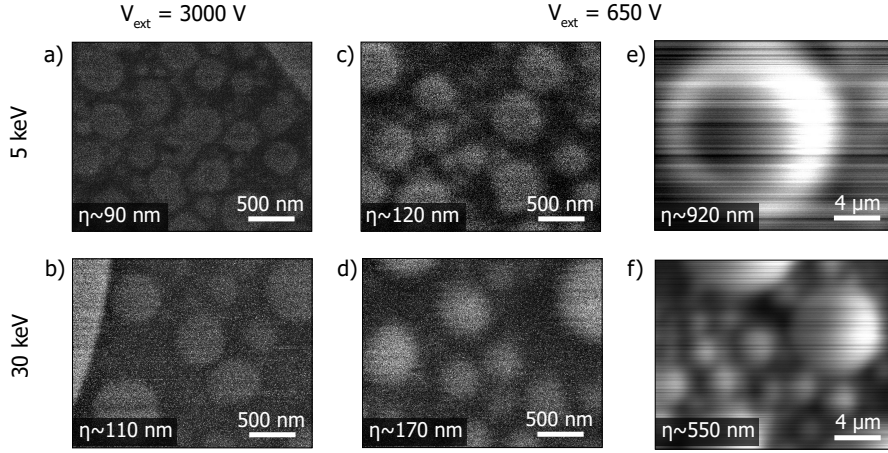


Figure 2.7: Secondary electron images of a Sn ball sample using a pulsed electron beam at 5 keV (top row) and 30 keV (bottom row). (a-b) Images obtained using $V_{\text{ext}} = 3000 \text{ V}$ and $60 \mu\text{m}$ aperture. (c-d) Images obtained using $V_{\text{ext}} = 650 \text{ V}$ and $60 \mu\text{m}$ aperture. (e-f) Images obtained under conditions for the highest electron current ($V_{\text{ext}} = 650 \text{ V}$ and 1 mm aperture).

A critical parameter for a good spatial resolution is the initial region of the tip from which electrons are emitted. The smaller this area, the tighter we can focus the electron beam on the sample. Given a certain brightness of the source, which is determined by the conditions of electron emission, a reduction of the emitted area results also in a decrease of the electron current (Eq. 2.1). Hence, there is always a tradeoff between high spatial resolution and signal, which in our case is either secondary electrons (SE) or CL.

A way of keeping a relatively small emitting area is by using a high suppressor and extractor voltages, as discussed above. Even when using the same value of V_{ext} as in continuous mode, we need to readjust C_1 for optimum resolution, both due to the thermal contraction of the tip when lowering its temperature (see 2.4.2) and difference in the photoemission area with respect to continuous emission. In experiments, it is usually more convenient to lower the extractor voltage to 3000 V, which allows us to fully suppress continuous emission (see section 2.4.2) while keeping a relatively high extractor field. Figure 2.7a shows an SE image of Sn balls obtained using $V_{\text{ext}} = 3000 \text{ V}$ and a 5 keV electron beam, for which we extract a spatial resolution of $\eta \sim 90 \text{ nm}$. Here we used a $60 \mu\text{m}$ aperture and condenser lens $C_1 = 760 \text{ V}$, obtaining a current of 0.3 pA. Fig. 2.7b shows an image obtained using the same extractor voltage but at 30 keV ($C_1 = 1220 \text{ V}$, $I = 5 \text{ pA}$, $\eta \sim 110 \text{ nm}$).

Working at a very low extractor voltage (magnitude comparable to the suppressor voltage, $V_{\text{supp}} = 500 \text{ V}$) can pose some advantages, such as a larger electron current and smaller energy width, as discussed in 2.5.3. However, the larger collection efficiency of electrons, as discussed in section 2.5.3 results in a larger area from

which electrons are emitted, thus effectively reducing the brightness of the source. Figs. 2.7c,d show images obtained at low extractor voltage ($V_{\text{ext}} = 650\text{ V}$) at 5 and 30 keV. Here we also used a $60\text{ }\mu\text{m}$ aperture and obtained a spatial resolution of $\eta \sim 120\text{ nm}$ at 5 keV ($C_1 = 200\text{ V}$, $I = 0.5\text{ pA}$) and $\eta \sim 170\text{ nm}$ at 30 keV ($C_1 = 600\text{ V}$, $I = 7\text{ pA}$). Finally, in applications that require a high electron current, we can tune the conditions at low extractor voltage such that a large portion of the emitted current reaches the sample, but at the expense of a very poor spatial resolution. Figs. 2.7e, f show images obtained also at low extractor using a 1 mm aperture, meaning that a big fraction of the photoemitted electrons reach the sample. In these cases we obtained a large electron current ($\sim\text{ nA}$) but at the expense of much lower spatial resolution: $\eta \sim 920\text{ nm}$ at 5 keV ($I = 1\text{ nA}$, $C_1 = 450\text{ V}$) and $\eta \sim 550\text{ nm}$ at 30 keV ($I = 1.2\text{ nA}$, $C_1 = 1000\text{ V}$).

Space-charge effects can also impact the spatial resolution for pulses containing multiple electrons. It is therefore desirable to keep a low number of electrons per pulse when possible. On the one hand, the width of the electron beam can be broadened due to Coulomb repulsion, thus directly increasing the size of the electron spot on the sample plane. Moreover, spherical aberrations might become more important due to this widening of the beam. Finally, the electron optics also suffer from chromatic aberrations, given that electrons with slightly different energies will be focused in different planes. Hence, the large energy spreads obtained for a high number of electrons per pulse (section 2.5.3) will have a negative impact on the spatial resolution. We should note that effects due to Coulomb repulsion are most important when the initial emitting area is small, such as in the high extractor case. When having a very low extractor voltage, the widening of the electron beam due to space-charge effects, and spherical and chromatic aberrations, might be negligible compared to the already large initial spot size.

The spatial resolutions obtained from these measurements are larger than the highest ones reported for other USEMs ($\sim 5\text{ nm}$), in which a Schottky FEG source and a laser with similar characteristics as ours were used [90]. Here we discuss the main factors that can contribute to this discrepancy and possible improvements. We should note that there are different methods to quantify the size of the electron beam on the sample from a given SE image, each yielding different values [119]. Hence, the definition of spatial resolution between different works can differ, thus making it difficult to precisely compare values derived using different techniques. The value of the extractor voltage can play an important role in the spatial resolution, due to the difference in effective emission area from the electron source, as we have discussed above. Hence, a high extractor voltage, ideally the same as in continuous mode, should be used when high spatial resolution is needed. A resolution of $\sim 35\text{ nm}$ using our initial USEM was reported when using a high extractor voltage [49].

A major source of loss in spatial resolution can come from the settings of the electron column, including working distance, electron optics and column alignment. In our measurements we used a working distance of 14 mm , corresponding to the one at which CL measurements are performed, instead of the optimum one

for our SEM (~ 10 mm). This effect could be reduced by using an SEM designed for optimum performance at such working distance. The settings of the electron optics, including condenser lenses (C_1 and C_2) and gun tilt/shift, need to be optimized for each value of electron energy and extractor voltage. The process of optimization of C_1 and C_2 requires readjusting the focus and astigmatism of the beam at each condenser value, which can result in some uncertainty in the final optimum values of C_1 and C_2 . A systematic study of the optimum condenser values, including different sets of experiments to account for differences in beam alignment, could help improve the current settings. Additionally, ensuring an optimum mechanical alignment of the electron column is important to achieve a high spatial resolution. Finally, as we have already discussed above, there is a tradeoff between spatial resolution and electron current on the sample, and a low current results in a small SE signal. In these cases, the optimization of focus and astigmatism on the sample becomes challenging.

Overall, the analysis of spatial resolution reported in this section serves as a guide to understand the parameters that play a role in the resolution and the different regimes in which the USEM can operate. Further improvements, such as the ones proposed above, could be developed to bring the spatial resolution towards the 5–10 nm range.

2.7. TEMPORAL RESOLUTION

Finally, a key parameter in a laser-driven SEM is its temporal resolution. Here we estimate and set an upper limit for the pulse width of the electron on the sample, and we show an application of time-resolved CL in the USEM.

2.7.1. ELECTRON PULSE WIDTH

The electron pulse width (Δt_{e^-}) has two contributions: the laser pulse width (Δt_{laser}) and the temporal spread due to the electron energy distribution ($\Delta t_{\Delta E}$). The latter is due to the fact that the arrival time of electrons on the sample depends on their kinetic energy. As we have previously shown, the electron energy distribution is strongly affected by Coulomb repulsion between electrons from the same pulse. The electron temporal spread taking into account space-charge effects is typically calculated using Monte-Carlo simulations or mean-field theory, among others [63, 102, 117, 118, 120–122]. For simplicity, here we assume that the energy spread due to Coulomb repulsion takes place instantaneously after emission, which is reasonable given the low energy and high temporal and spatial concentration of electrons around the source [102, 118]. We also assume that the photoemission process is instantaneous compared to the rest of timescales. Hence, the temporal broadening happens during the acceleration phase of the electron beam up to the desired electron energy E_0 , and while the beam propagates along the rest of the microscope column, where no external voltage is applied. In this case, the

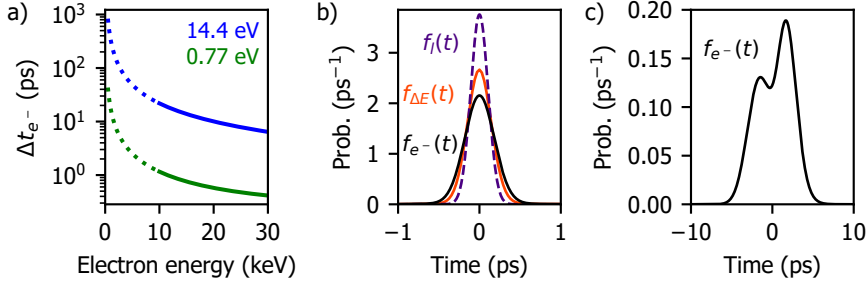


Figure 2.8: Calculated temporal spread of electron pulses. (a) Electron pulse width Δt_{e^-} as a function of the final electron beam energy for initial energy distributions of 0.77 and 14.4 eV (green and blue, respectively). The calculations were performed using Eq. 2.6. (b) Temporal distribution of the laser ($f_l(t)$) (purple curve, $\Delta t_{\text{laser}} = 250$ fs), temporal spread of a 30 keV electron pulse ($f_{\Delta E}(t)$) only due to the initial energy distribution of $\Delta E = 0.77$ eV measured for ~ 0.53 electrons per pulse (orange, $\Delta t_{\Delta E} = 330$ fs) and the convolution of both (black, $f_{e^-}(t)$), corresponding to the final electron pulse temporal shape ($\Delta t_{e^-} = 416$ fs). (c) Temporal distribution of the electron pulse obtained for the initial energy distribution obtained from the measurements in Fig. 2.6b ($\Delta E = 14.4$ eV for 1029 electrons per pulse), resulting in a spread of $\Delta t_{e^-} = 6.4$ ps.

temporal width of the electron pulse is given by [63]

$$\begin{aligned} \Delta t_{e^-} &\approx \sqrt{\Delta t_{\text{laser}}^2 + \Delta t_{\Delta E}^2} = \\ &= \sqrt{\Delta t_{\text{laser}}^2 + \frac{m}{2E_i} \Delta E_i^2 \left[-\frac{d}{E_0} \left(1 - \frac{v_i}{v_f} \right) - \frac{l}{m\gamma_f^3 v_f^3} \right]^2}. \end{aligned} \quad (2.6)$$

Here, E_i is the energy of the electrons right after being emitted from the cathode, from which we can extract $v_i = \sqrt{\frac{2E_i}{m}}$, and ΔE_i is their initial energy spread, which we will consider the same as the total energy spread measured in section 2.5.3 (ΔE).

The final speed of the electron is represented by $v_f = \gamma_f \sqrt{\frac{2E_0}{m}}$, where γ_f corresponds to the Lorentz contraction factor, m is the electron mass, d indicates the distance between the tip apex and the accelerating anode and l is the length from the accelerating anode to the sample plane.

From Eq. 2.6 it follows that the temporal spread is directly determined by the final electron beam energy: at lower operating voltages the initial energy spread plays a larger role than at higher voltages. Figure 2.8a shows the temporal width of the electron pulse as a function of the final electron beam energy, calculated using Eq. 2.6. The two curves represent two different initial energy spreads, 0.77 and 14.4 eV (green and blue, respectively), corresponding to the lowest and largest distributions measured with the RFA (Fig. 2.6). In the calculations we considered $d = 25$ mm, $l = 0.5$ m, $\Delta t_{\text{laser}} = 250$ fs, and an electron initial energy given by $E_i = E_f + \phi_{\text{ZrO/W}} = 14.37$ eV, thus assuming that the reduction of the energy barrier due to the extractor voltage is negligible. This assumption is reasonable given that

the experiments were performed using a low extractor field ($V_{\text{ext}} = 650\text{V}$). As expected, the lowest temporal spread, corresponding to $\Delta t_{e^-} = 416\text{fs}$, is obtained at the highest electron beam energy (30 keV) and for the lowest initial energy spread. We should note that the results obtained for electron beam energies lower than 10 keV are less precise, due to the design of the SEM. In these cases, electrons are initially accelerated to 10 keV and subsequently decelerated down to the desired final energy. Hence, Eq. 2.6 should be modified to include additional terms for the deceleration and acceleration steps. Instead, for energies larger than 10 keV, the electrons are directly accelerated to their final energy.

Using a similar derivation as for Eq. 2.6, we can calculate the distribution of arrival time of electrons within a pulse, given a known energy distribution (see [63]). Figures 2.8b,c show the temporal shape of an electron pulse containing an average of 0.53 and 1029 electrons per pulse, obtained assuming the initial energy distributions from Figs. 2.6a,b ($\Delta E = 0.77$ and 14.4eV , respectively). In order to avoid extra calculations for the deceleration at lower operating energies, which would obscure the trends investigated here, we performed the calculations for an electron beam energy of 30 keV. We assume that the energy distributions obtained with the RFA measurements at 5 keV are still valid at larger energies, which is reasonable given that it is typically assumed that space-charge effects dominate before the acceleration of electrons [102]. Fig. 2.8b shows the distribution of arrival time of electrons for the case of a low number of electrons per pulse ($N_e = 0.53$). The orange curve represents the electron temporal spread exclusively due to the initial energy distribution ($\Delta t_{\Delta E} = 330\text{fs}$), while the pulse width of the laser is shown in purple ($\Delta t_{\text{laser}} = 250\text{fs}$, dashed curve). The convolution of both curves gives the electron pulse distribution (black curve), for which we obtain a temporal width of $\Delta t_{e^-} = 414\text{fs}$. For larger number of electrons per pulse, the contribution of the laser pulse is negligible and the electron pulse shape is mostly determined by the energy spread due to space-charge effects, as shown in Fig. 2.8c. In this case we obtain an electron pulse width of $\Delta t_{e^-} = 6.4\text{ps}$. We should emphasize that these numbers are rough approximations, given the assumptions taken, but give an idea of the magnitude of the effect of Coulomb repulsion on the overall time resolution.

Given that the retrieved temporal pulse widths are relatively small, direct measurements of the electron pulse width are typically performed by means of pump-probe techniques, such as in photon-induced near-field electron microscopy (PINEM) [65] or when analyzing the change in SE signal due to photogenerated carriers [98]. In our setup we can perform time-resolved cathodoluminescence (CL) measurements using a time-correlated single-photon counting (TCSPC) technique. In brief, the CL emitted by the sample is collected using a parabolic mirror and guided to a $105\mu\text{m}$ fiber (Thorlabs FG105UCA), from which it is focused on a single-photon avalanche detector (PicoQuant PDM Series), which is connected to a time-correlator (PicoQuant PicoHarp 200). The 2nd harmonic of our fs laser ($\lambda = 517\text{nm}$) is detected by a photodiode (PicoQuant TDA 200) also connected to the time-correlator, thus serving as a trigger. Further information on the CL setup and TCSPC measurements is provided in chapter 3 (section 3.4.3). Figure 2.9 shows a measurement

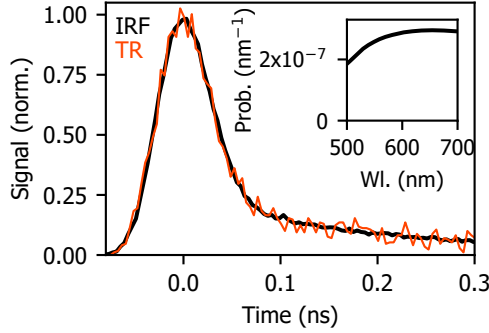


Figure 2.9: Time resolution of a time-resolved CL experiment. The time resolution of the TCSPC detection system is measured by acquiring a time trace of the fs-laser (black curve), corresponding to ~ 60 ps. The orange curve shows the decay statistics of transition radiation on a Au sample when exciting with a 30 keV pulsed electron beam (650 ± 100 electrons per pulse). The TR emission was spectrally filtered in the 620 ± 5 nm range. Inset: theoretical calculation of the spectrum of emission probability for TR per electron and spectral bandwidth. Wl.: wavelength.

obtained when directly sending the 2nd harmonic ($\lambda_{\text{exc}} = 517$ nm) of the fs laser into the TCSPC setup (black curve). Given that the laser pulse width is ~ 250 fs, the curve indicates the resolution of our detection system (IRF), which we find to be $\Delta t_{\text{IRF}} \approx 60$ ps.

Figure 2.9 also shows the decay statistics of transition radiation (TR) obtained after excitation of a single-crystal Au sample with a 30 keV electron beam (650 ± 100 electrons per pulse, $V_{\text{ext}} = 650$ V, $C_1 = 1050$ V, 1 mm aperture) (orange curve). In the experiment we used a 620 ± 5 nm bandpass filter to avoid temporal spread due to dispersion in the fiber, given the broad spectral emission of TR. A theoretical calculation of the spectrum of TR is shown in the inset of Fig. 2.9 [25]. TR emission can be considered as instantaneous (~ 20 fs [31]), thus the decay statistics are dominated by the TCSPC response function (Δt_{IRF}) and electron pulse width (Δt_e). We find that the time trace of TR matches well with the resolution of this method measured with the laser. From this experiment we can set an upper limit for the electron pulse width of ~ 10 ps, in agreement with the maximum pulse width estimated from the electron energy spread, as described above (6.4 ps). The upper limit is estimated by accounting for errors in the fitting procedure and differences between experimental sets.

2.7.2. APPLICATION: CL LIFETIME MAP

One of the advantages of performing time-resolved CL measurements is the ability to study the electron excitation and photon emission dynamics at the nanoscale. Hence, we tested our USEM by studying a GaN nanowire containing five vertically-aligned InGa_N/GaN quantum wells [42]. An SE image of the nanowire is shown in Figure 2.10a, which was obtained using a 10 keV continuous electron beam. Fig.

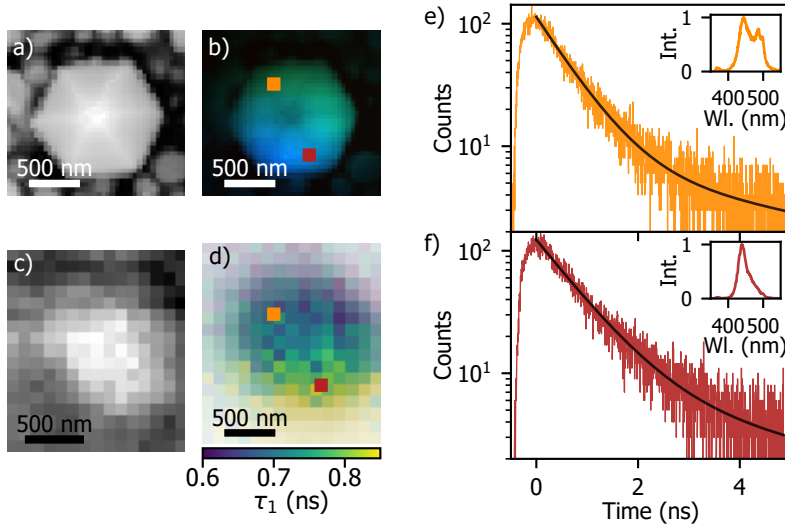


Figure 2.10: CL lifetime maps of InGaN/GaN quantum wells embedded in a GaN nanowire. (a) SE image of the top of the nanowire obtained with a 10 keV continuous electron beam. (b) False-color RGB map of the CL emission, obtained with a continuous electron beam. (c) SE image of the same nanowire obtained in pulsed conditions ($V_{ext} = 650 \text{ V}$, $\sim 5 \text{ pA}$). (d) Lifetime map of the nanowire, in which the colorscale indicates the fast component of the decay (τ_1) and the transparency reflects the amount of signal collected in each pixel. (e, f) Examples of time traces obtained at the positions indicated in (d). The decays are fitted with a double exponential function (black curves). Inset: CL spectra obtained at the two positions indicated in (b). Abbreviations: WL. is wavelength and Int. is intensity.

2.10b shows a false-color RGB CL map, obtained by dividing the spectral range in three color channels: blue (corresponding to emission in the 400 – 450 nm range), green (450 – 500 nm) and red (500 – 550 nm). We observe that CL emission is not uniform on the nanowire, but there is a slight red-shift in the top region compared to the bottom one. This difference in spectra is clearly observed in the insets of Figs. 2.10e, f, showing two spectra taken at the positions on the nanowire indicated in Fig. 2.10b. The spectrum obtained on the top part of the nanowire exhibits two peaks centered around 440 nm and 490 nm, while the one corresponding to the bottom part of the nanowire exhibits a single peak at 440 nm.

Next, we measured the temporal CL statistics as a function of electron beam position. Fig. 2.10c shows the SE image obtained in pulsed conditions. In this case we used $V_{ext} = 3000 \text{ V}$, $C_1 = 885 \text{ V}$ and $60 \mu\text{m}$ aperture. The laser repetition rate was set to 25.19 MHz and we used a laser energy of 29 pJ, resulting in an electron current of $I \sim 5 \text{ pA}$. The spatial resolution is clearly worse than in the continuous case, which could be improved by further reducing the electron current, but at the expense of a lower CL signal. Figs. 2.10e,f show two examples of traces obtained at two different positions on the nanowire, corresponding to approximately the same positions as for the spectra in the inset. Here the CL signal was optically filtered

with a 500 nm shortpass filter. The solid curves represent the fits obtained when fitting the time traces with a double-exponential decay, defined as

$$f(t) = S(A_1 e^{-t/\tau_1} + A_2 e^{-t/\tau_2}). \quad (2.7)$$

Here τ_1 and τ_2 are the characteristic lifetimes for each exponential, S is the total amplitude of the curve and A_1 and A_2 are the corresponding weights of each exponential ($A_2 = 1 - A_1$). We obtain that the decay from the traces can be fitted with a fast ($\tau_1 \approx 0.7$ ns) and a slow ($\tau_2 \approx 7.5$ ns) component. Fig. 2.10d shows a map of τ_1 , in which the color scale represents the extracted value of τ_1 , and the transparency of each pixel indicates the CL intensity and weight of this decay compared to τ_2 . We obtain a value of $\tau_1 \approx 0.6$ ns on the top-left of the nanowire, while the measurements on the bottom part of the nanowire exhibit a slightly slower decay, $\tau_1 \approx 0.85$ ns. Figure 2.11a shows the map obtained for the second characteristic decay, τ_2 , which does not exhibit a clear spatial dependence. Fig. 2.11 also shows the relative contributions of each decay component (b and c, respectively) as a function of the position on the nanowire. The lack of spatial features suggests that both decay components are equally present on the different positions of the nanowire, with the main spatial dependence being in the value of the fast decay τ_1 . In order to elucidate the origin of this spatial dependence we should perform further experiments and analysis, which are beyond the scope of this section. This experiment shows that we can perform quantitative time and spatially-resolved CL measurements using a pulsed electron beam, despite the lower spatial resolution.

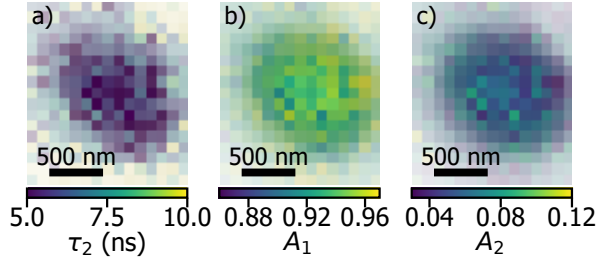


Figure 2.11: Lifetime map fits of InGaN/GaN quantum wells in a GaN nanowire. Spatial maps of the slow decay (τ_2 , a) and weights of the fast and slow decays (A_1 and A_2 , b and c respectively). The parameters correspond to the variables in Eq. 2.7.

2.8. CONCLUSION

In this chapter we have presented the design and characterization of a laser-driven USEM. In the first part of the chapter we have discussed the fundamental emission process of a Schottky FEG in continuous and pulsed modes, together with the technical implementation of our USEM. Next, we have used a retarding field analyzer to measure the energy spread of continuous and pulsed electron beams. We

show that the energy spread of a continuous electron beam is strongly influenced by the temperature of the electron cathode, decreasing from 1.86 to 0.59 eV, in accordance with the Schottky FEG emission theory. In the case of a pulsed electron beam, we observe a clear increase of the energy spread with increasing number of electrons per pulse, which is attributed to the effect of Coulomb repulsion between electrons from the same pulse. We obtain energy spreads ranging from 0.77 eV for an average of less than one electron per pulse, up to 14.4 eV for more than 1000 electrons per pulse. We characterize the spatial resolution of our USEM, obtaining a resolution of around ~ 90 nm in the limit of low current on the sample (≤ 1 pA), and we discuss the possible differences between our experiment and other studies, in which higher spatial resolutions are obtained. We show that decreasing the extractor voltage results in a loss of spatial resolution but increase of electron current, thus offering an alternative solution for applications in which a high electron current is critical. Finally, we discuss the time resolution of our time-resolved SEM and CL measurements. From the measurements of energy spread we estimate an electron pulse width of 416 fs for pulses containing less than one electron, on average, in which case the electron temporal resolution is limited by the laser pulse width. In the case of more than 1000 electrons per pulse, we calculate a widening of the electron pulse width up to 6.4 ps. The time resolution in CL experiments is ~ 60 ps, limited by the detection system. The feasibility of our USEM to perform time-resolved CL experiments is evaluated by showing an example of CL measurements on nanowires containing InGaN/GaN quantum wells.

